PROCEEDINGS OF SPIE SPIEDigitalLibrary.org/conference-proceedings-of-spie Linear Stokes measurement of thermal targets using compact LWIR spectropolarimeter

Conference Paper · May 2020

DOI: 10.1117/12.2557887

CITATION
1

READS
58

4 authors, including:

Meredith Kupinski
The University of Arizona
42 PUBLICATIONS **218** CITATIONS

SEE PROFILE

PROCEEDINGS OF SPIE

SPIEDigitalLibrary.org/conference-proceedings-of-spie

Linear Stokes measurement of thermal targets using compact LWIR spectropolarimeter

Hart, Kira, Kupinski, Meredith, Wu, Dong, Chipman, Russell

Kira A. Hart, Meredith Kupinski, Dong Wu, Russell A. Chipman, "Linear Stokes measurement of thermal targets using compact LWIR spectropolarimeter," Proc. SPIE 11412, Polarization: Measurement, Analysis, and Remote Sensing XIV, 114120H (22 May 2020); doi: 10.1117/12.2557887

SPIE.

Event: SPIE Defense + Commercial Sensing, 2020, Online Only, California, United States

Linear Stokes measurement of thermal targets using compact LWIR spectropolarimeter

Kira A. Hart[a], Meredith Kupinski[a], Dong Wu[b], and Russell A.Chipman[a]

[a]University of Arizona, 1630 E University Blvd, Tucson, USA
[b]NASA Goddard Spaceflight Center, 8800 Greenbelt Rd, Greenbelt, USA

ABSTRACT

The trade-off between spectral resolution and instrument throughput is analyzed for a compact, uncooled, long-wave infrared (LWIR) channeled spectropolarimeter (IRCSP). The IRCSP was developed as a part of the Sub-mm Wave and InfraRed Polarimeters (SWIRP) project out of NASA's Goddard Spaceflight Center. The IRCSP scientific objective targets measurements of AOLP and DOLP with 1-μm spectral resolution from 8.5 - 12.5 μm in a single snapshot. The geometry of the field stop determines the field of view (FOV) of the IRCSP. This work relates the spectral resolution, instrument throughput, and polarimetric accuracy of a spectro-polarimeter to the FOV. The accuracy of linear Stokes retrievals for low temperature thermal targets are predicted for varying FOV and measurement noise conditions. This work presents a method to quantify the achievable accuracy in AOLP and DOLP as a function of field stop dimensions and signal-to-noise ratio (SNR). While smaller field stops are shown to improve accuracy as the spectral resolution is increased, low SNR is the dominant source of error for the IRCSP prototype. For the IRCSP, a SNR of at least 80 is required to produce DOLP measurements with $< 5\%$ error for targets with DOLP < 0.2.

Keywords: LWIR, polarimetry, polarization, remote sensing, spectro-polarimeter

1. INTRODUCTION

Channeled-polarimeters are an effective and demonstrated method to produce instantaneous hyperspectral polarimetric data without sacrificing spatial resolution.[1–8] To accomplish this, thick birefriengent crystals are utilized to alter the input polarization state as a function of wavelength. The thickness of these crystals is chosen such that the dispersion creates a variation in retardance across the measured waveband.[1] For linear channeled polarimeters, a combined quarter wave retarder (QWR) and a thick birefringent crystal act as a wavelength dependent circular retarder, rotating the incident linear polarization. The output rotated light is then modulated using a polarizing optical element and measured by a spectrometer.[5–7,9] For polarized input, cosinusoisal intensity fringes with a period determined by the net retardance difference across the measured bandwidth are measured by spectrometer.[10] Linear polarization can then be measured with a spectral resolution equivalent to the period of modulation produced by the birefringent elements.[1] Channeled polarimetry is particularly attractive for space based applications and snapshot polarimetry because it requires no moving components.[3,5] As a result, channeled polarimeters have a demonstrated history of remote sensing applications; the SPEX airborne hyper-spectral multi-angle polarimeter has demonstrated success utilizing a channeled polarimeter for aerosol characterization.[2–4,8,9,11]

While polarimetric imaging in the visible bands has become wide-spread in recent years to enhance target detection, interesting polarization signatures also exist in the long-wave infrared (LWIR).[12–15] Often referred to as the thermal IR, this waveband generally encompasses 7 - 13 μm where thermal radiation from terrestrial objects is at a maximum. Due to thermal emission, the LWIR polarimatric signal contains variable combinations of emission and reflection signatures depending on the thermal content of the objects in and outside the detection field of view.[15] This phenomenology produces opportunities to perform passive target detection at night, detect oil on water, locate underground landmines, and more.[5,7,13] Until recently, the development of compact LWIR

Further author information: (Send correspondence to Kira Hart)
Kira Hart.: E-mail: khart@optics.arizona.edu

Polarization: Measurement, Analysis, and Remote Sensing XIV, edited by David B. Chenault, Dennis H. Goldstein,
Proc. of SPIE Vol. 11412, 114120H · © 2020 SPIE · CCC code: 0277-786X/20/$21 · doi: 10.1117/12.2557887

polarimeters was limited by cooling requirements for bolometer detectors. The now widespread availability of uncooled microbolometer detectors with noise equivalent temperature differences (NEDT) < 50 mK has opened the door for compact LWIR polarimetry. Polaris Sensor Systems has shown success utilizing these uncooled detectors in a LWIR linear Stokes camera by applying a microfilter array close to the microbolometer focal plane.[13,16]

The IRCSP developed in this work is a compact, uncooled, LWIR channeled polarimeter and is a part of the Submm-Wave and Long Wave InfraRed Polarimeters for Cirrus Ice Properties (SWIRP) project out of NASA Goddard Spaceflight Center. Previously, a global polarimetric study of ice crystals was performed by the Global Precipitation Measurement Microwave Imager (GMI) which investigated H-V polarization variances in the 89 and 166 GHz channels.[17] This mission attained great success demonstrating the the ability to constrain particle shape factor, however uncertainty in density and size significantly impacted results.[17] To reduce uncertainty in ice water path and crystals with smaller effective diameters, higher frequency polarimetric measurements are needed.[17,18] Recently, *Coy et al* have shown that LWIR linear polarization measurements are particularly sensitive to ice crystal in optically thin clouds.[19] To retrieve these microphysical properties, linear Stokes measurements with 1-μm spectral resolution and radiometric accuracy of $\leq$ 1K from 8 - 12.5 μm are required. This corresponds to error of less than 5% in DOLP for ice temperature targets. The SWIRP project adapts these science requirement to a rapidly deployable CubeSat architecture following guidance from the 2017 ESTO Decadal Survey.[20,21] To meet the technical and scientific objectives for the SWIRP mission, channeled polarimetry is combined with uncooled LWIR imaging technology to build a linear Stokes polarimeter with a volume of less than 120 mL (.12 CubeSat U).[10,21]

To support performance analysis of the prototype IRCSP, two separate instruments have been constructed. The first was delivered to GSFC in 2019 for integration into the larger SWIRP assembly, and a second clone instrument, IRCSP2, was constructed for testing at the University of Arizona. The field stop geometry is the only difference between these instruments: 100 μm for the IRSCP and 30 μm in the IRSCP2. As the dimension of the field stop increases, spectral blurring is introduced at the focal plane. This not only reduces the spectral resolution, but blurs the modulation used for polarimetric retrievals, making a small field stop optimal to minimize this effect. For the IRCSP, this is complicated by the reduced radiance of targets at ice temperatures. As the dimension of the field stop is reduced and the spectral resolution improves, the throughput of the instrument and subsequent SNR at the focal plane will be reduced. This work evaluates how changes in the dimension of the field stop and SNR affect the accuracy of polarimetric measurements produced by the IRCSP. Measured polarimetric performance, transmission, and efficiency of the constructed IRCSP are used to build a Mueller matrix model which describes the continuous operation of the system as a function of wavelength. This is combined with a continuous to discrete model to evaluate the dependence of polarimetric accuracy on SNR and field stop dimensions to inform cost-benefit analysis for future engineering decisions.

2. INSTRUMENT CONCEPT

2.1 Linear Stokes Polarimetry

The Stokes parameters uniquely quantify the polarization state of incoherent light with four numbers: $\mathbf{S} = [S_0, S_1, S_2, S_3]$. The first component, S_0, is the total radiance, and the other components also have units of radiance. The definitions of linear Stokes parameters S_1 and S_2 are associated with a given coordinate system. The normalized Stokes parameters $\mathbf{s} = \mathbf{S}/S_0 = [1, s_1, s_2, s_3]$ are similarly represented by lower case $\mathbf{s}$. Circular polarization S_3 is typically negligible for sunlight scattered by the atmosphere or Earth's surface.[22] The linear Stokes components are often combined into a dimensionless quantity, the degree of linear polarization (DOLP)

$$\text{DOLP} = \rho = \frac{\sqrt{S_1^2 + S_2^2}}{S_0} = \frac{I_{pol}}{A} \tag{1}$$

where I_{pol} is the polarized radiance (the fraction of light in the scene that is polarized) and $A = S_0$ is the total radiance.[23] The angle of linear polarization (AOLP) is

$$\text{AOLP} = \theta = \frac{1}{2}\tan^{-1}\left(\frac{S_2}{S_1}\right). \tag{2}$$

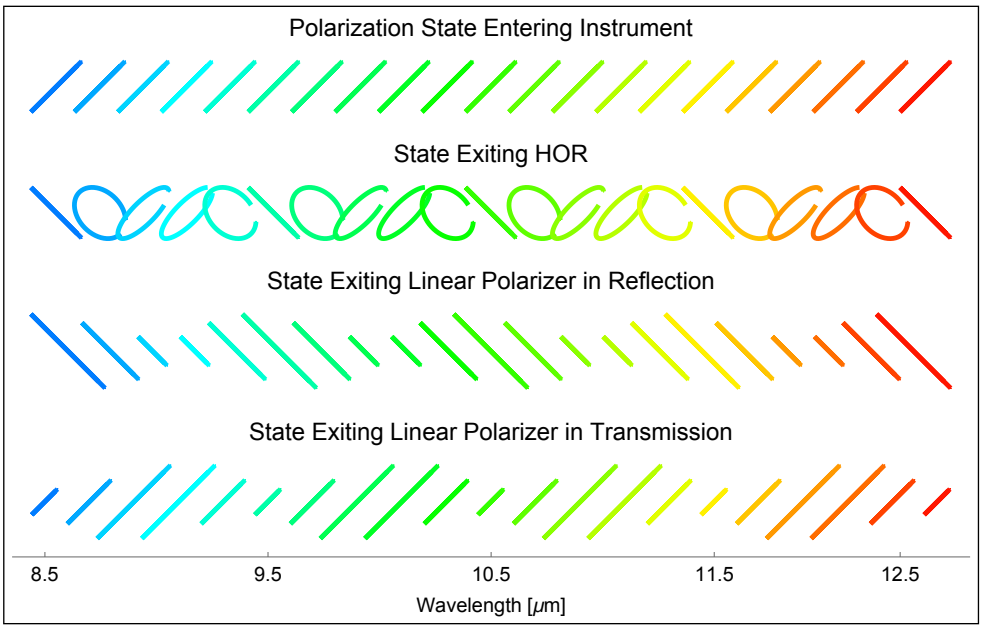

Figure 1: The transformation of linearly polarized light with constant DOLP and AOLP as propagated through the IRCSP Mueller matrix model. The polarization is altered as a function of wavelength as it passes through the QWR and HOR. Following the HOR the beam is split and modulated by a linear polarizer in reflection and transmission.

Note that DOLP is invariant to the coordinate system but AOLP depends on the coordinate system. A 3×1 linear Stokes vector is expressed in terms of A, ρ, and θ by

$$\mathbf{S}(\lambda) = A_\lambda[1, \rho_\lambda cos2\theta_\lambda, \rho_\lambda \sin 2\theta_\lambda]^t \tag{3}$$

where t denotes transpose.[23] Here, A_λ is the spectral intensity of the target and both AOLP: θ_λ and DOLP:ρ_λ are functions of wavelength.

2.2 Dual Path Channeled Polarimetry

A channeled polarimeter has three major components: a system of retarders to operate on the incident polarized light as a function of wavelength, a polarizing element to modulate the spectrally varying state in intensity, and an imaging spectrometer to measure the modulated spectrum with respect to wavelength. For the IRCSP, a quarter wave retarder (QWR) and thick birefringent CdSe high order retarder (HOR) combine to form a wavelength dependent circular retarder. The thickness of the CdSe was chosen to produce 4 periods of modulation from 8.5 -12.5 μm.[10] Following the HOR, a linear polarizer (LP) is used as a polarizing beam splitter to produce two modulated channels with a $\pi/2$ phase offset. The operation of the polarizing elements for incident linearly polarized light can be seen in a Figure 1. Two blazed diffraction gratings and uncooled microbolometer cameras follow the LP, which constitute the spectrometer for the IRCSP. To produce a radiometric and polarimetric measurement in the presence of rapidly varying intensity, as is produced by the absorption of ozone in the atmosphere, the output of both reflection and transmission of the LP must be taken. Added together, the two orthogonal spectra measure the radiance of the target. This dual path approach has previously been demonstrated by *van Harten et. al* to maintain accuracy in spectral line polarimetry.[11]

The polarimetric behavior of the system can be described by a Mueller matrix model.[23] For the IRCSP, the ideal Mueller matrix model for the dual path in trasmission from the LP is described

$$\frac{1}{2}\begin{bmatrix}1&0&1&0\\0&0&0&0\\1&0&1&0\\0&0&0&0\end{bmatrix}\begin{bmatrix}1&0&0&0\\0&1&0&0\\0&0&\cos\left(\frac{2\pi\delta}{\lambda}\right)&\sin\left(\frac{2\pi\delta}{\lambda}\right)\\0&0&-\sin\left(\frac{2\pi\delta}{\lambda}\right)&\cos\left(\frac{2\pi\delta}{\lambda}\right)\end{bmatrix}\begin{bmatrix}1&0&0&0\\0&0&0&-1\\0&0&1&0\\0&1&0&0\end{bmatrix}\begin{bmatrix}1\\\rho\cos(2\theta)\\\rho\sin(2\theta)\\0\end{bmatrix} = \frac{1}{2}\begin{bmatrix}1+\rho\sin\left(\frac{2\pi\delta}{\lambda}-2\theta\right)\\0\\1+\rho\cos\left(\frac{2\pi\delta}{\lambda}-2\theta\right)\\0\end{bmatrix} \tag{4}$$

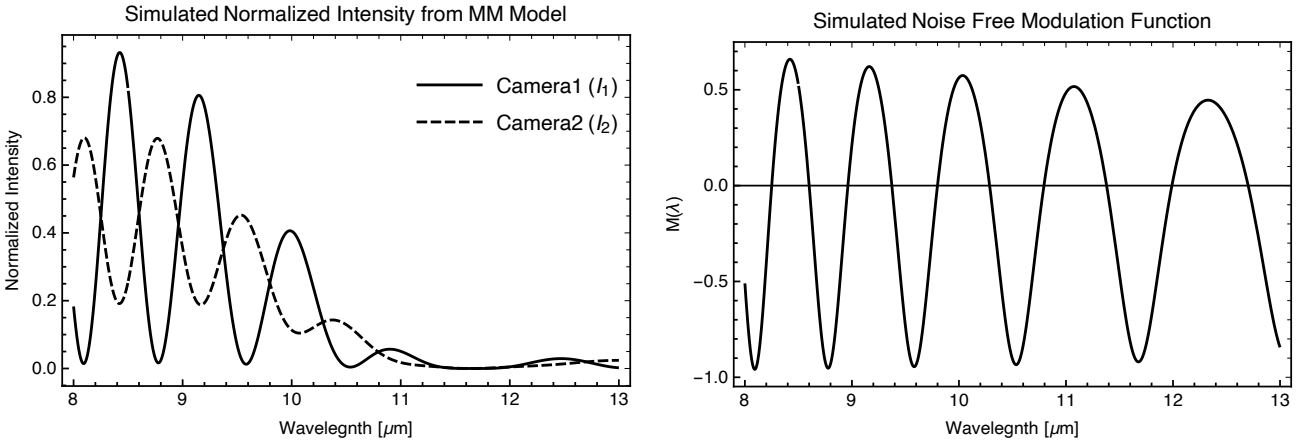

(a) Normalized Intensity (b) Modulation Function

Figure 2: Simulated noise free modulation function: (a) the intensity in path 1 and 2, (b) the modulation function. The frequency of modulation is proportional to $1/\lambda$ due to the dispersion of CdSe. Reduced contrast from the linear polarizer in reflection causes the modulation function to be reduced.

where the matrices from left to right correspond to the LP, HOR, and QWR respectively and δ is the retardance from the HOR. The produced intensity, a function of wavelength as seen on the LHS of the equation, is a sinusoidal function with frequency δ whose amplitude corresponds to the incident DOLP and phase represents the AOLP.

Every Mueller matrix has wavelength dependence. Non-ideal wavelength dependent variations in retardance, diattenuation, transmission, and grating efficiency are expected. The intensity I_c produced by the system including these deviations is described

$$I_c(\rho,\theta,\lambda) = \frac{1}{2}A_\lambda \alpha(\lambda,\theta)\beta_c(\lambda)\left[\Sigma_c(\lambda) \pm \Delta_c(\lambda)\rho_\lambda\left[\epsilon(\lambda)cos2\theta_\lambda \sin\left(\frac{2\pi\delta(\lambda)}{\lambda}\right) + cos\left(\frac{2\pi\delta(\lambda)}{\lambda}\right)\sin 2\theta_\lambda\right]\right] \quad (5)$$

where the $\pm$ is addition for the transmitted $c = 1$ path and subtraction for the reflected $c = 2$. Transmission and efficiency terms are combined as $\alpha(\lambda,\theta)$ for the polarization dependent transmission occurring upstream of the LP, and $\beta_c(\lambda)$ is path dependent transmission following the LP. Deviation from the ideal retardance in the QWR is $\epsilon(\lambda)$. The maximum transmission and reflection of the LP are denoted $T^{\max}$, $T^{\min}$, $R^{\max}$ and $R^{\min}$. These are combined $\Sigma_1 = T^{\max} + T^{\min}$, $\Delta_1 = T^{\max} - T^{\min}$, $\Sigma_2 = R^{\max} + R^{\min}$, and $\Delta_2 = R^{\max} - R^{\min}$. During narrowband calibration, 9 parameters: $\alpha(\lambda,\theta)$,$\beta_c(\lambda)$, $\Sigma_c(\lambda)$,$\Delta_c(\lambda)$,$\epsilon(\lambda)$,$\delta(\lambda)$ are fit to calibration measurements at varying incident AOLPs and wavelengths. The calculated coefficients fully describe the polarimetric behavior of the IRCSP.[10]

While the Mueller matrix model describes polarimetric behavior, it does not characterize artifacts introduced by the discrete pixel sampled measurements at the focal planes. In addition to deviations from the ideal Mueller matrix model, spectral blurring of the diffracted wavelengths at the focal plane is a source of error. Consider the spatial distribution of a monochromatic diffracted order $f_c(\lambda_l, x)$ at the focal plane. A combination of the diffraction grating's quality and the field stop geometry determine the overlap of this distribution for adjacent wavelengths. In a pixel-sampled continuous to discrete model, the monochromatic intensity given by the Mueller matrix model in Eq. 5 can be expressed as a summation of broadband noise-free measurements

$$P_{c,j}(\rho,\theta) = \sum_{l=0}^{L} I_c(\rho,\theta,\lambda_l)\int_{x_j}^{x_{j+1}} f_c(\lambda_l, x)dx \quad (6)$$

where $P_{c,j}$ is a noise-free measurement from camera c and pixel j. Each noise-free measurement is an incoherent sum of L wavelengths λ_l that contribute to pixel j where the pixel has an active area pitch of $x_{j+1} - x_j$. To

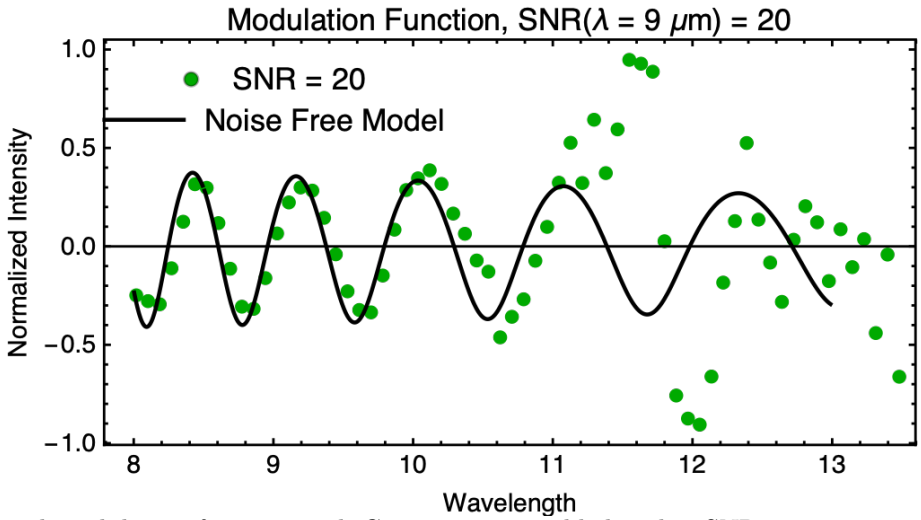

Figure 3: Simulated modulation function with Gaussian noise added with a SNR = 20 at 9 μm. Reduced SNR at longer wavelengths is compounded when applying Eq. 7

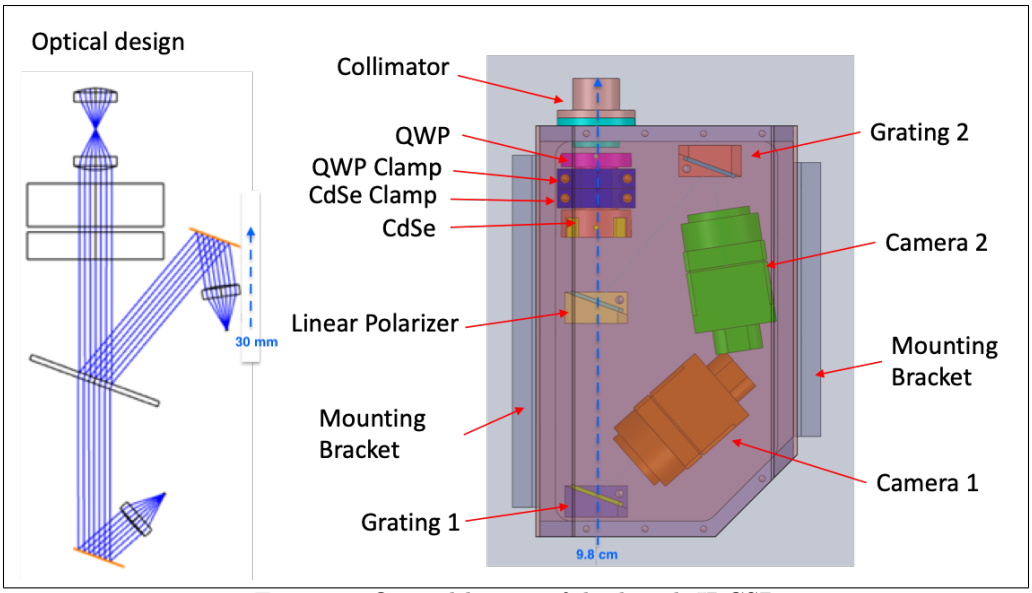

Figure 4: Optical layout of dual path IRCSP

estimate an intensity $\hat{I}_c(\lambda_l)$ at wavelength samples λ_l, a spatial average is computed over the range of $f_c(\lambda_l, x)$. In Eq. 6 the modulation of $I_c(\rho, \theta, \lambda_l)$ is effectively blurred by broadband incident light.

To characterize spectral blurring, the SPEX polarimeter defined a modulation function

$$M(\lambda_l) = \frac{\hat{I}_1(\lambda_l) - \hat{I}_2(\lambda_l)}{\hat{I}_1(\lambda_l) + \hat{I}_2(\lambda_l)} = W(\lambda_l)\left[S_1 cos\left(\frac{2\pi\delta(\lambda_l)}{\lambda_l}\right) - S_2 \sin\left(\frac{2\pi\delta(\lambda_l)}{\lambda_l}\right)\right] \tag{7}$$

where $W(\lambda)$ is termed the polarimetric efficiency, and $\delta(\lambda)$ is the carrier frequency in Eq.5.[2,11] A noise-free simulation of $\hat{I}_c$ and associated modulation function are shown in Figure 2. The phase of $M(\lambda)$ depends on the AOLP, and the amplitude depends on both the polarimetric efficiency and DOLP. Due to dispersion, the frequency of modulation is higher at lower wavelengths.

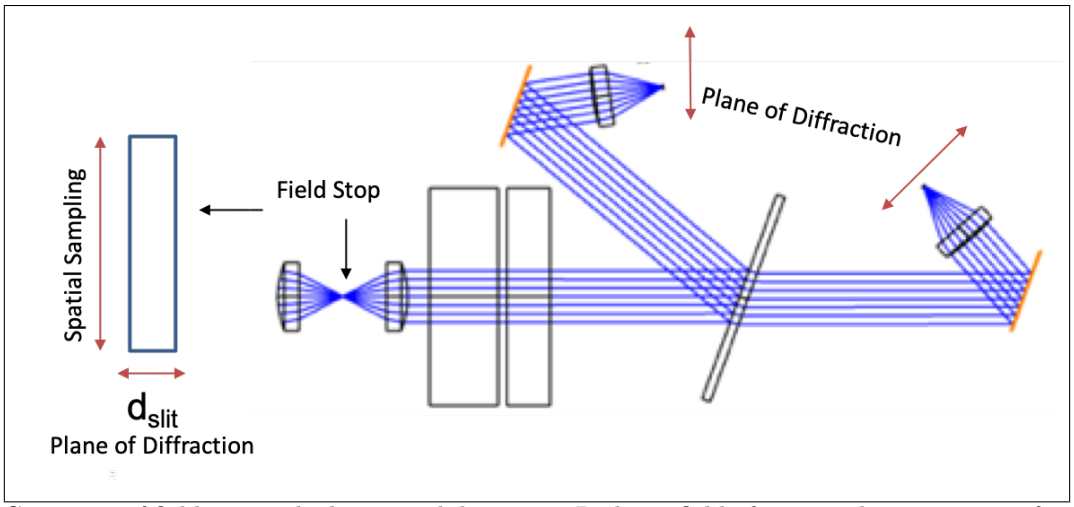

Figure 5: Geometry of field stop. The horizontal dimension Reduces field of view, reduces severity of polarization aberrations from off axis light, and dictates the spectral resolution. The vertical dimension dictates the spatial sampling.

2.3 Optical Design

A dual path channeled polarimeter approach was chosen to maintain radiometric and polarimetric accuracy across the waveband.[10,11] While it is necessary to measure both paths to correct for atmospheric attenuation, there are several drawbacks to the dual path approach employed in this design. Ideally, a single camera configuration would eliminate the error introduced by adding 2 sources of uncorrelated detector noise from the 2 cameras. In addition, the linear polarizer's varied performance in reflection and transmission introduces a significant artifact as is seen in Eq. 5. While single detector solutions such as a Wollaston prism were explored, these approaches posed too high an engineering, timeline, and supply-chain risk. The linear polarizer approach was chosen to minimize risk and demonstrate the IRCSP instrument concept.

To meet the tight spatial requirements introduced by the targeted .12 U instrument volume, detector selection was limited. FLIR's Boson uncooled microbolometer was chosen for its 2.1 × 2.1 × 1 cm footprint. However, the detector has not been previously demonstrated in a spectral imaging application, nor was spectral response information for the camera available at the time of purchase. During the calibration of the first IRCSP, the response of the detector was found to drop off significantly past 11 μm.[10] The detector's limited spectral response at longer wavelengths is ultimately the limiting factor in the instrument's performance. The performance of the detector is also impacted by the temperature of the surrounding environment. In addition to the modulated spectrum, the camera images the surrounding thermal environment onto the detector. While some of this stray thermal light can be mitigated with baffling, some broadband thermal background signal will always be present. This effect is reduced by lowering the temperature of the instrument as a whole. In space- or high altitude flight, this is done passively, and the SNR at the focal plane for all wavelengths is expected to increase. Environmental chamber testing to quantify this improvement is the subject of ongoing work as the IRCSP is integrated into the larger SWIRP instrument.

The choice of optical elements was driven by performance, availability, and form-factor requirements. CdSe was selected as the birefringent material for the HOR due to its thermal stability and well documented performance in the LWIR. An off-the-shelf cadmium thiogallate zero order wave-plate from Edmund Optics was purchased as the QWR. The HOR was designed to produce 4 waves of variation in retardance across 8.5-12.5 μm. The crystal was manufactured and AR coated by Gooch and Housego in Ohio.

2.4 Field Stop

The front aperture of the system consists of 2 collimating lenses with a field stop. This assembly serves to reduce stray light in the system, limit systemic polarization introduced by collimating lenses, and match the

	IRCSP	IRCSP2
Field stop geometry	$100\mu m$ diameter pinhole	$30\mu m$ in plane of diffraction
SNR at 9 μm	100	30
SNR at 11 μm	10	5
Width of diffracted order	6 pixels	3 pixels
trade-off	Higher throughput	Increased spectral resolution

Table 1: Comparison of design trade-offs for slit installed in original IRCSP and IRCSP2. Cited SNR is for a target at 1000°C.

spatial resolution of the IRCSP to that of the sub-mm instruments. The field stop dimension perpendicular to the plane of diffraction (Figure 5) dictates the instrument's spatial field of view in the spatial sampling direction. Note that the IRCSP only performs spatial sampling in the direction perpendicular to the plane of diffraction and the instrument must be operated in a push-broom scanning motion to image in the direction parallel to the plane of diffraction. The field stop dimension parallel to the plane of diffraction, d_{slit}, dictates the instrument throughput, field of view in the scanning direction, and spectral resolution. While this work focuses predominantly on throughput and spectral resolution, it is true that as d_{slit} increases in dimension, so does the field of view in the direction of the push-broom scan. The optimal field of view will change depending on the geometry of the instrument deployment. For the final integration of the SWIRP instrument, the optimal choice matches the footprint of the IRCSP to that of the sub-mm instruments on-board.

The shape and extent of the diffracted orders for a given field stop dimension are calculated using ray-tracing software. For the analysis presented in this work, we assume that the effect of polarization dependent transmission is negligible compared to the reduction in polarimetric efficiency from spectral blurring and linear polarizer contrast. The first IRCSP was built with a a 100 μm pinhole to maximize throughput. In contrast, the IRCSP2 was constructed with a slit field stop with a 30 μm extent in the plane of diffraction. Figure 6 shows the pixel extent of a diffracted order for a narrow-band light source for slit dimensions corresponding to the IRCSP and IRCSP2. The diffracted order for the IRCSP2 is near ideal and has a width of just over one pixel, maximizing the spectral resolution. While the width of the diffracted order for the IRCSP is larger, the throughput will be increased and thus the SNR will be improved. Table 1 summarizes the resulting SNR and design trade-offs for the two constructed instruments.

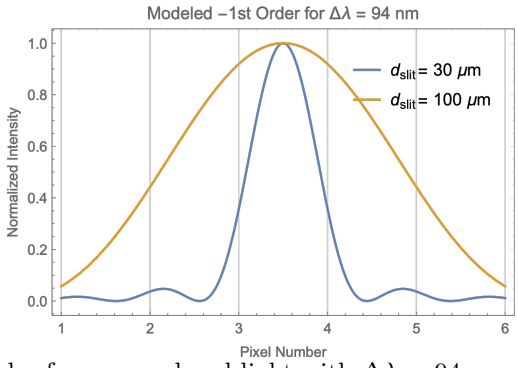

Figure 6: Size of the diffracted order for narrow band light with $\Delta\lambda = 94nm$ produced at the focal plane for slit dimensions $d_{slit} = 30\mu m$ and $d_{slit} = 100\mu m$. Spectral resolution is maximized when the extent of the diffracted orders is $<$ one pixel

3. METHODS

3.1 Instrument Characterization

In January 2020, the clone IRCSP2 was delivered to NASA Goddard Space Flight center for narrow-band characterization. To evaluate the response of the system as a function of wavelength, a testbed with a monochromator and blackbody source at 1,000 °C was utilized. All tests were performed with the IRCSP at room temperature.

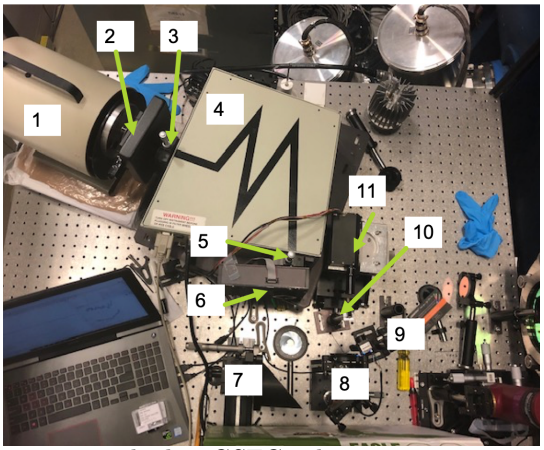

Figure 7: Layout of the monochromator testbed at GSFC. The components are 1. Black Body Source, 2. Optical Chopper, 3. Monochromator input slit, 4. Monochromator, 5. Output slit, 6. Spectral filter wheel, 7. Off-axis parabolic mirror, 8. Fold Mirror , 9. Reference detector, 10. Linear polarizer on rotating mount, 11. IRCSP.

For all measurements the monochromator was operated with a slit size corresponding to a spectral resolution of 94 nm. The output of the monochromator can be assumed to be unpolarized.

To characterize the polarization-dependent response of the system, a rotating linear polarizer was placed between the monochromator output and the instrument's aperture. The tabletop setup with the linear polarizer is shown in Figure 7. The linear polarizer was rotated to produce measurements with DOLP = 1 and AOLP $\in [0°, 180°]$ for 100 wavelengths between 8 and 13 μm. As a result, spectral blurring is minimized and the polarimetric performance of the system is sampled with a narrow-band illumination. These data are fit to Eq. 5 to produce an estimate of the instrumental polarization terms. The measured continuous Mueller matrix model of the IRCSP is then given by

$$\hat{I}_c(A_\lambda, \rho, \theta, \lambda) = \frac{1}{2} A_\lambda \hat{\alpha}(\lambda, \theta) \hat{\beta}_c(\lambda) \left[\hat{\Sigma}_c(\lambda) \pm \hat{\Delta}_c(\lambda) \rho_\lambda \left[\hat{\epsilon}(\lambda) cos 2\theta_\lambda \sin \hat{\delta}(\lambda) + cos \hat{\delta}(\lambda) \sin 2\theta_\lambda \right] \right] \tag{8}$$

where $\widehat{hat}$ terms represent those calculated during the monochromator calibration. This measured MM model is used for all subsequent simulations.

3.2 Continuous to Discrete Model

To simulate the pixel sampled intensity at the focal plane, a functional form for $f_c(d_{slit}, \lambda_l, x)$ from Eq. 6 must be estimated for a given slit size d_{slit}. The location of the center diffracted order for a given wavelength is determined using the monochromator calibration for each camera. To then determine the shape of the diffracted order, a ray-trace is performed to produce the functional shape as in Figure 6. Then, the raw pixel intensity $P_{c,j}$ at pixel j is calculated

$$P_{c,j}(A, \rho, \theta, d_{slit}) = \sum_{l=0}^{L} \tilde{I}_c(A, \rho, \theta, \lambda_l) \int_{x_j}^{x_{j+1}} f_c(d_{slit}, \lambda_l, x) dx \tag{9}$$

where I_c is the continuous intensity calculated using Eq. 8. For this simulation, $\lambda_l = 8\mu m + l\Delta\lambda$, $\Delta\lambda = 0.05\mu m$, L =100, and the spectral intensity $A_\lambda = 1$ is chosen to be constant and normalized across the spectrum.

Next, noise is added with a selected signal-to-noise (SNR) ratio. The SNR is defined as the mean over variance of the signal at the pixel corresponding to 9 μm for an unpolarized input,

$$\text{SNR} = \frac{\bar{P}_{c,j=9\mu m}(1, 0, 0, d_{slit})}{\text{Var}(P_{c,j=9\mu m}(1, 0, 0, d_{slit}))} \tag{10}$$

where $P_{c,j}$ is as defined in Eq. 9. The Gaussian sampled noise $\eta(\text{SNR})$ is a randomly sampled Gaussian, centered at $P_{c,j=9\mu m}(1,0,0,d_{slit})$ with a width of $\text{Var}(P_{c,j=9\mu m}(1,0,0,d_{slit}))$. The simulated pixel values are then calculated

$$\mathbf{P}_j(\rho,\theta,\text{SNR},d_{slit}) = P_{c,j}(1,\rho,\theta,d_{slit}) + \eta(\text{SNR}) \tag{11}$$

3.3 Wavelength Assignment

A process called wavelength assignment associates the pixel sampled spectrum at the focal plane with a given wavelength. Each pixel j_{λ_i} is associated with the wavelength λ_i centered on it, determined during monochromator calibration. The averaged response value at that wavelength is then calculated as the average over the adjacent pixels for broadband light

$$C_c(\rho,\theta,\text{SNR},d_{slit},\lambda_i) = \frac{1}{N}\sum_{j_{\lambda_i}-N/2}^{j_{\lambda_i}+N/2} \mathbf{P}_{c,j_{\lambda_i}}(\rho,\theta,\text{SNR},d_{slit}) \tag{12}$$

where N is the number pixels averaged over, and $\mathbf{P}_{c,j_{\lambda_i}}(\rho,\theta,\text{SNR},d_{slit})$ is given in Eq. 11.

3.4 Simulated Calibration

The final step in data processing before polarimetric retrieval is to associate the raw response values calculated in Eq. 12 with radiometric units. This correction is dependent on the choice of slit size d_{slit} and must be calculated for each slit configuration. To do this, broadband calibration data is simulated for each slit size. In calibration, many frames will be averaged over, so noise is assumed to be minimized. First, a radiometric correction is performed using an unpolarized calibration. Since we assume that the input spectral radiance A_λ is constant, the radiometric correction in each path $\mathbf{r}_c$ is

$$\mathbf{r}_c(\lambda_i) = 1/C_c(\rho,\theta,\text{SNR},d_{slit},\lambda_i) \tag{13}$$

where C_c is the response value from Eq. 12. This is then used to produce an array of normalized intensity measurements for any given input

$$\mathbf{I}_c(\rho,\theta,\text{SNR},d_{slit}) = \frac{1}{2}\mathbf{r}_c C_c(\rho,\theta,\text{SNR},d_{slit},\lambda_i). \tag{14}$$

The polarimetric behavior of the instrument is calibrated by fitting broadband measurements with DOLP=1 and AOLP $\in [0,\pi]$ to the modulation function in Eq. 7 as a function of AOLP. To calibrate the virtual system, these measurements are simulated using Eq. 14 and the modulation function is calculated at each AOLP. Then, at each wavelength, the data is fit to Eq. 7 as a function of θ to estimate the polarimetric efficiency $\hat{\mathbf{W}}$. Thus, the measurement equation at each wavelength is

$$\mathbf{M}_{\lambda_l} = \hat{\mathbf{W}}_{\lambda_l}\left[s_{1,\lambda_l}\cos\left(\frac{2\pi\delta(\lambda_l)}{\lambda_l}\right) - s_{2,\lambda_l}\sin\left(\frac{2\pi\delta(\lambda_l)}{\lambda_l}\right)\right]. \tag{15}$$

3.5 Demodulation

For broadband light, the DOLP and AOLP is determined by fitting the measured modulation vector $\hat{\mathbf{M}}$ to the measurement function in Eq. 15 using the calculated calibrated polarimetric efficiency vector $\hat{\mathbf{W}}$. The fit is performed over $1\mu m$ windows to calculate the estimated Stokes parameter

$$\hat{\mathbf{s}} = \left(1, \hat{\rho}\cos(2\theta), \hat{\rho}\sin(2\hat{\theta}), 0\right). \tag{16}$$

To evaluate the accuracy in polarimetric retrievals for a given SNR and field stop configuration, the measured intensity for a randomly input Stokes parameter $\mathbf{s}$ is generated using Eq. 14 and the modulation function is

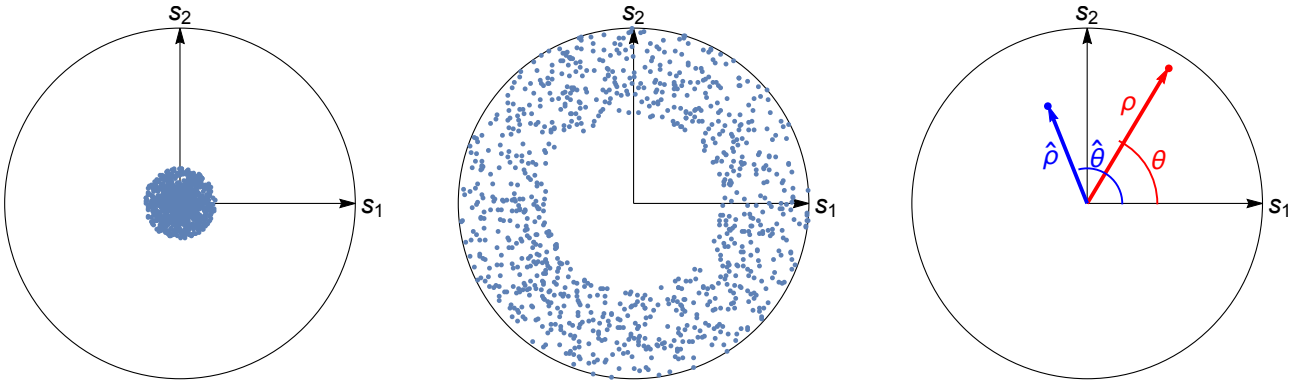

(a) Low DOLP (b) High DOLP (c) Simulated retrieval

Figure 8: Simulation of retrieval for randomly generated Stokes parameters. 2 cases are examined: (a) low DOLP ($0 \leq$ DOLP $< .2$) and high DOLP ($.5 <$ DOLP ≤ 1). (c) shows an example difference in input $\mathbf{s} = (1, \rho\cos(2\theta), \rho\sin(2\theta), 0)$ and retrieved $\hat{\mathbf{s}} = (1, \hat{\rho}\cos(2\theta), \hat{\rho}\sin(2\hat{\theta}), 0)$.

computed. Then the retrieved Stokes vector $\hat{\mathbf{s}}$ is calculated. The error in DOLP σ_ρ is then calculated as the normalized difference in magnitude between the input and retrieved Stokes vectors

$$\sigma_\rho = \frac{||\mathbf{s}|| - ||\hat{\mathbf{s}}||}{||\mathbf{s}||} \tag{17}$$

and the AOLP error is

$$\sigma_\theta = \cos^{-1}\left(\frac{\mathbf{s}\cdot\hat{\mathbf{s}}}{||\mathbf{s}\cdot\hat{\mathbf{s}}||}\right) \tag{18}$$

where σ_θ is the angle between input and retrieved linear states.[24]

4. RESULTS

Retrievals were simulated for 50 randomly generated Stokes parameters, all permutations of 20 different SNRs $\in [10, 200]$, and 20 slit dimensions $d_{slit} \in [20\mu m, 120\mu m]$. Low (Fig. 8a) and high (Fig. 8b) DOLP cases are considered, as error is expected to be greater for lower DOLPs where the amplitude of modulation is reduced. RMSE for DOLP and AOLP are shown in Figures 9 and 10; for low and high DOLPs, respectively. The RMSE is computed for polarimetric retrievals at the $1 - \mu m$ band centered on 9 μm, as this is the band with highest response for the IRCSP. The SNR of the camera is lower at longer wavelengths so the RMSE reported at 9 μm is a lower bound for performance at longer wavelengths.

For both high and low input DOLP, the AOLP retrieval is more accurate than the DOLP retrieval. The AOLP is estimated from the phase of the modulated measurements. Phase estimates are most robust to noise than amplitude estimates. Since AOLP retrievals are less susceptible to noise, the effect of spectral blurring for larger slit dimensions is more evident as seen in Figures 9b and 10b . For both AOLP and DOLP retrievals, the worst performance occurs in bottom left corner of the plots where the field stop is at its largest and SNR is at its lowest. For DOLP retrieval, the SNR is more critical than slit size for accurate retrievals. Figures 9a and 10a show that regardless of slit dimension, error in DOLP retrieval is $< 5\%$ for SNR > 80 in low DOLP retrievals, and SNR > 40 in high DOLP retrievals. As anticipated, the lowest error in retrievals for DOLP and AOLP for both cases occurs in the top right corner of the plots where SNR is maximized and slit size is minimized.

Retrievals for input Stokes parameters with low DOLP in Figures 9a and 9b show more error than those with high DOLP in Figures 10a and 10b. Since the DOLP produced by atmospheric scattering is expected to be low, accuracy in low DOLP retrievals is essential to meet the scientific objective. To reliably produce polarimetric retrievals with DOLP error $\sigma_\rho < 5\%$, the system would need to achieve SNR > 100 across the bandwidth for the IRCSP2 and SNR > 140 for the IRCSP. For the smallest $d_{slit} = 20\mu m$, SNR> 80 is required to meet the objective. Thus, achieving increased SNR across the bandwidth is critical.

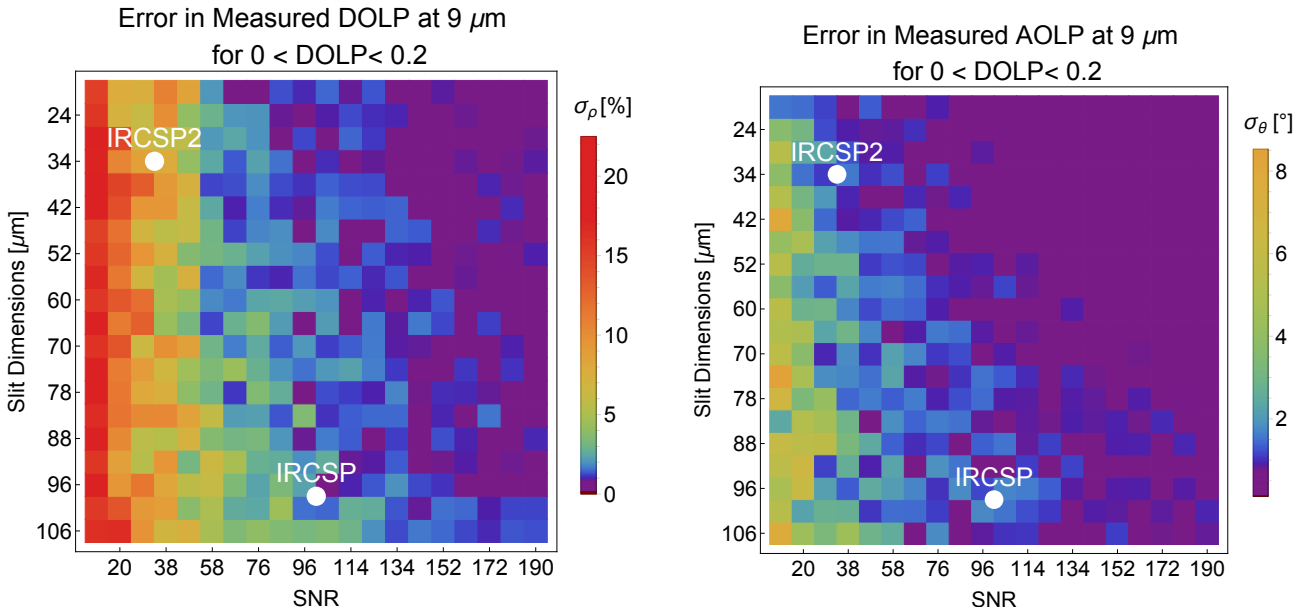

(a) Error in DOLP

(b) Error in AOLP

Figure 9: RMSE in (a) DOLP from Eq. 17 and (b) AOLP from Eq. 18 for randomly generated Stokes parameters with $0 \leq \text{DOLP} < .2$ computed as a function of slit dimensions and SNR. 50 retrieval trials were used for each slit/SNR configuration. The SNR and field stop dimension for the IRCSP and IRCSP2 are labeled for targets at $1000°C$.

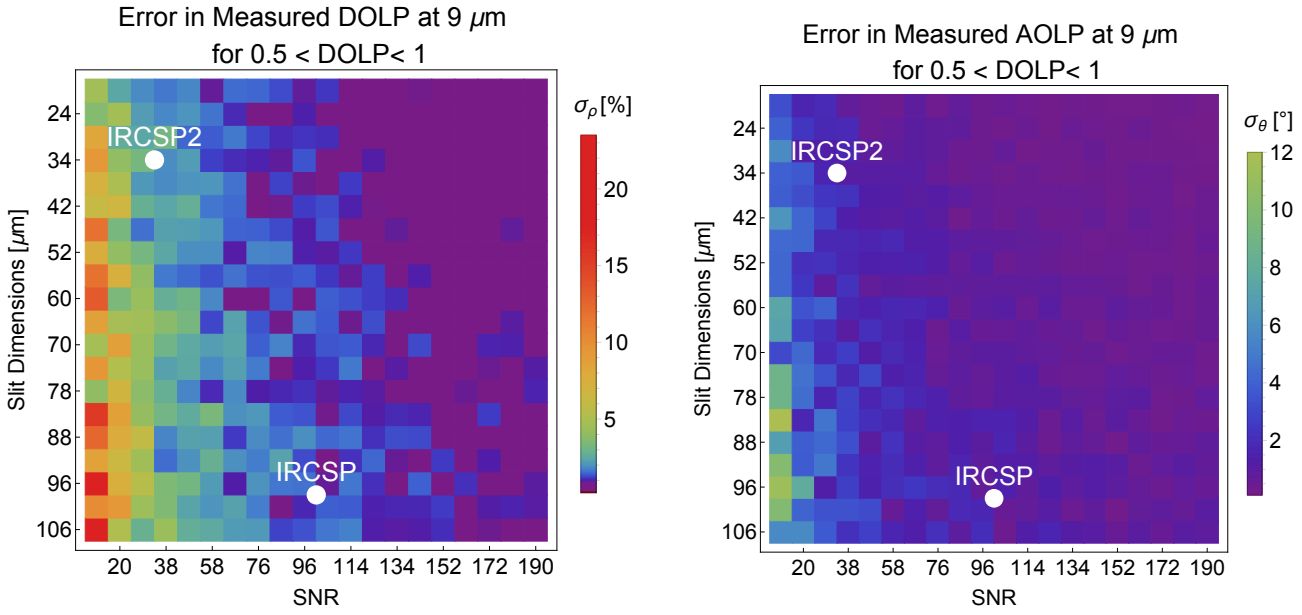

(a) Error in DOLP

(b) Error in AOLP

Figure 10: RMSE in (a) DOLP from Eq. 17 and (b) AOLP from Eq. 18 for randomly generated Stokes parameters with $0.5 < \text{DOLP} \leq 1$ computed as a function of slit dimensions and SNR. 50 retrieval trials were used for each slit/SNR configuration. The SNR and field stop dimension for the IRCSP and IRCSP2 are labeled for targets at $1000°C$.

5. CONCLUSION

This work has implemented a computational method to simulate the accuracy of a linear channeled polarimeter as a function of the spectral resolution and SNR. First, the construction of a virtual instrument with variable field stop dimensions is built through the combination of measured optical element performance and a pixel sampled continuous to discrete model. Then, an ensemble of randomly generated Stokes parameters was input to the virtual instrument for possible combinations of SNR and field stop dimension to determine retrieval accuracy.

The results show that for the instrument at room temperature, the measured SNR of both the IRCSP and IRCSP2 will be insufficient to meet the scientific objective of less than 5% error in DOLP. While improvements in spectral resolution improve retrieval accuracy for high SNR measurements, low SNR is the predominant source of retrieval error. To achieve $\sigma_\rho < 5\%$, the SNR of the instrument must be greater than 80 for any slit dimension. While the larger d_{slit} improved the SNR of the IRCSP in comparison to the IRSCP2, the improvement is still insufficient. Environmental chamber tests will determine how the instrument SNR varies and improves as the ambient temperature is lowered. As passive cooling is possible for the IRCSP during spaceflight, it is plausible that the reduction of thermal background from lower ambient temperatures will be sufficient. As microbolometer technology continues to improve, it may be possible in the near future to replace the FLIR Boson with a more sensitive detector.

While this work evaluated the IRCSP performance as it pertains to the SWIRP scientific objective, applications of this technology are not limited to ice cloud measurement. For applications such as surface normal estimation or discrimination between metal and dielectric thermal targets, accuracy in AOLP may be more important than DOLP, and an appropriate field stop may be chosen using this analysis. Since the field stop can be readily exchanged in the IRCSP instrument assembly, different field stops can be installed for different imaging tasks. Once a target accuracy in DOLP and AOLP are determined, the appropriate field stop dimensions and required SNR can be determined using the generated results.

ACKNOWLEDGMENTS

The authors acknowledge the NASA Earth, Science, and Technology Office for funding this work. The authors would like to thank collaborators at NASA Goddard Spaceflight Center: Giovanni De Amici, Aaron Pearlman, Peter Pantina, and Manuel Vega. The IRCSP prototypes and opto-mechanical designs were made possible thanks to work done at the University of Arizona by Chang Jin Oh and the Large Optics Testing and Fabrication facility. Finally, the authors thank Jeremy Parkinson and James Heath for their assistance with data collection and characterization of the IRCSP2.

REFERENCES

[1] Oka, K. and Kato, T., "Spectroscopic polarimetry with a channeled spectrum," *Optics Letters* **24**(21), 1475–1477 (1999).

[2] Smit, J. M., Rietjens, J. H., van Harten, G., Di Noia, A., Laauwen, W., Rheingans, B. E., Diner, D. J., Cairns, B., Wasilewski, A., Knobelspiesse, K. D., et al., "Spex airborne spectropolarimeter calibration and performance," *Applied optics* **58**(21), 5695–5719 (2019).

[3] Rietjens, J., Smit, J., Di Noia, A., Hasekamp, O., Van Harten, G., Snik, F., and Keller, C., "Spex: a highly accurate spectropolarimeter for atmospheric aerosol characterization," in [*International Conference on Space Optics—ICSO 2014*], **10563**, 1056344, International Society for Optics and Photonics (2017).

[4] Rietjens, J. H., Smit, M., van Harten, G., Di Noia, A., Hasekamp, O. P., de Boer, J., Volten, H., Snik, F., and Keller, C. U., "Accurate spectrally modulating polarimeters for atmospheric aerosol characterization," in [*Polarization Science and Remote Sensing VII*], **9613**, 96130S, International Society for Optics and Photonics (2015).

[5] Iannarilli, F. J., Shaw, J. A., Jones, S. H., and Scott, H. E., "Snapshot lwir hyperspectral polarimetric imager for ocean surface sensing," in [*Polarization Analysis, Measurement, and Remote Sensing III*], **4133**, 270–284, International Society for Optics and Photonics (2000).

[6] Iannarilli, F. J., Jones, S. H., Scott, H. E., and Kebabian, P. L., "Polarimetric-spectral intensity modulation (p-sim): enabling simultaneous hyperspectral and polarimetric imaging," in [*Infrared technology and applications XXV*], **3698**, 474–482, International Society for Optics and Photonics (1999).

[7] Craven-Jones, J., Way, B. M., Hunt, J., Kudenov, M. W., and Mercier, J. A., "Thermally stable imaging channeled spectropolarimetry," in [*Polarization Science and Remote Sensing VI*], **8873**, 88730J, International Society for Optics and Photonics (2013).

[8] Snik, F., Rietjens, J. H., Van Harten, G., Stam, D. M., Keller, C. U., Smit, J. M., Laan, E. C., Verlaan, A. L., Ter Horst, R., Navarro, R., et al., "Spex: the spectropolarimeter for planetary exploration," in [*Space Telescopes and Instrumentation 2010: Optical, Infrared, and Millimeter Wave*], **7731**, 77311B, International Society for Optics and Photonics (2010).

[9] Snik, F., Karalidi, T., and Keller, C. U., "Spectral modulation for full linear polarimetry," *Applied Optics* **48**(7), 1337–1346 (2009).

[10] Hart, K. A., Chipman, R. A., and Wu, D. L., "Compact lwir polarimeter for cirrus ice properties," **10655** (2018).

[11] van Harten, G., Snik, F., Rietjens, J. H., Smit, J. M., and Keller, C. U., "Spectral line polarimetry with a channeled polarimeter," *Applied optics* **53**(19), 4187–4194 (2014).

[12] Malone, N. R., Hampp, A., Gordon, E. E., Liguori, M. V., Thai, Y., Vodicka, J., and Bangs, J. W., "Detection comparisons between lwir and mwir polarimetric sensors," in [*Polarization: Measurement, Analysis, and Remote Sensing VIII*], **6972**, 69720P, International Society for Optics and Photonics (2008).

[13] Chenault, D. B., Vaden, J., Mitchell, D., and Demicco, E., "New ir polarimeter for improved detection of oil on water," *SPIE Newsroom* (2018).

[14] Chun, C. S., Fleming, D. L., Harvey, W., and Torok, E., "Polarization-sensitive thermal imaging sensors for target discrimination," in [*Targets and Backgrounds: Characterization and Representation IV*], **3375**, 326–336, International Society for Optics and Photonics (1998).

[15] Tyo, J. S., Ratliff, B. M., Boger, J. K., Black, W. T., Bowers, D. L., and Fetrow, M. P., "The effects of thermal equilibrium and contrast in lwir polarimetric images," *Optics express* **15**(23), 15161–15167 (2007).

[16] Chenault, D., Pezzaniti, L., Vaden, J., Roche, M., Michalson, J., and Gurton, K., "Pyxis: Enhanced Thermal Imaging with a Division of Focal Plane Polarimeter," tech. rep., Polaris Sensor Technologies, Inc (09 2015).

[17] Gong, J. and Wu, D. L., "Microphysical properties of frozen particles inferred from global precipitation measurement (gpm) microwave imager (gmi) polarimetric measurements," *Atmospheric Chemistry and Physics* **17**(4), 2741–2757 (2017).

[18] Miao, J., Johnsen, K.-P., Buehler, S., and Kokhanovsky, A., "The potential of polarization measurements from space at mm and sub-mm wavelengths for determining cirrus cloud parameters," *Atmospheric Chemistry and Physics* **3**(1), 39–48 (2003).

[19] Coy, J. J., Bell, A., Yang, P., and Wu, D. L., "Sensitivity analyses for the retrievals of ice cloud properties from radiometric and polarimetric measurements in sub-mm/mm and infrared bands," *Journal of Geophysical Research: Atmospheres* **n/a**(n/a), e2019JD031422 (2020). e2019JD031422 2019JD031422.

[20] ESTO, [*ESTO 2016 Report*], NASA (2016).

[21] Wu, D., Vega, M., Solly, M., Marrero, V., Hart, K., Guerrero, S., Gaines, W., Du Toit, C., De Amici, G., Deal, W., et al., "Swirp (submm-wave and long wave infrared polarimeter); a new tool for investigations of ice distribution and size in cyrrus clouds," in [*IGARSS 2019-2019 IEEE International Geoscience and Remote Sensing Symposium*], 8436–8439, IEEE (2019).

[22] Baum, B. A., Yang, P., Heymsfield, A. J., Bansemer, A., Cole, B. H., Merrelli, A., Schmitt, C., and Wang, C., "Ice cloud single-scattering property models with the full phase matrix at wavelengths from 0.2 to 100 μm," *Journal of Quantitative Spectroscopy and Radiative Transfer* **146**, 123–139 (2014).

[23] Chipman, R. A., Lam, T., and Young, G., [*Polarized Light and Optical Systems*], CRC Press, New York (2019 (first edition)).

[24] Kupinski, M., Chipman, R., and Clarkson, E., "Relating the statistics of the angle of linear polarization to measurement uncertainty of the Stokes vector," *Optical Engineering* **53**(11), 1 – 7 (2014).